Energy landscape of ZnO clusters and low-density polymorphs

Robabe Rasoulkhani,[1] Hossein Tahmasbi,[1] S. Alireza Ghasemi,[1] Somayeh Faraji,[1] Samare Rostami,[1] and Maximilian Amsler[2,*]

[1]*Department of Physics, Institute for Advanced Studies in Basic Sciences (IASBS), Zanjan 45137-66731, Iran*

[2]*Department of Materials Science and Engineering, Northwestern University, Evanston, Illinois 60208, USA*

(Received 16 February 2017; revised manuscript received 3 July 2017; published 14 August 2017)

We report on an extensive study of ZnO materials with cagelike motifs in clusters and bulk phases through structural searches using the minima hopping method. A novel putative ground state was discovered for the $(ZnO)_{32}$ cluster with a tubelike structure, closely related to the previously reported $(ZnO)_{24}$ ground-state cage geometry. Furthermore, the effect of ionization on the geometries and energetic ordering of $(ZnO)_n$ clusters with $n = 3$–$10,12$ was studied by directly sampling the energy landscape of the ionized system. Our results indicate that the transition from ring and planar structures to three-dimensional cages occurs at larger cluster sizes than in the neutral system. Inspired by the bottom-up design philosophy and the predominance of cagelike structures in medium-sized clusters, a search for crystalline ZnO was conducted aimed specifically at low-density polymorphs, resulting in the discovery of 57 novel metastable phases. The voids in these low-density materials closely resemble the hollow cage structures of small $(ZnO)_n/(ZnO)_n^+$ clusters with $n < 16$. Analogous to clathrate materials, these voids could serve to accommodate guest atoms to tailor the materials properties for various applications.

DOI: 10.1103/PhysRevB.96.064108

I. INTRODUCTION

Zinc oxide is one of the industrially most relevant inorganic compounds due to its versatile properties with applications as additives in rubbers, ceramics, and for pharmaceuticals [1–3]. At ambient condition, ZnO crystallizes in the thermodynamically stable wurtzite (WZ) structure with a direct and wide band gap of 3.37 eV [4,5], based on which it plays a key role in electronic and light-emitting devices. Due to its exciton binding energy of 60 meV, which exceeds the value of 21–25 meV in GaN, its strong room-temperature luminescence, exceptional transparency, and high electron mobility, ZnO has been considered a valuable optical material in the ultraviolet regime [6,7], with applications as transparent electrode in liquid crystal displays [8] and in energy-saving or heat-protecting windows [9].

Several other forms of ZnO beyond its crystalline ground-state structure have been reported with strongly varying materials properties. In nanoclusters, for example, the optical absorption depends crucially on their sizes and morphologies [10–12], and therefore a fundamental understanding of the structure-property relation and the growth mechanisms is essential to accurately tune the materials properties [13–15]. On the other hand, various metastable crystalline polymorphs of ZnO have been reported in the literature with properties different from the WZ phase. The high-pressure rock-salt (RS) phase [7,16] for example, which was recently recovered to ambient pressures [17,18], shows compelling thermoelectric properties with a promising figure of merit ZT in a wide temperature range [19]. Similarly, the zinc-blende (ZB) phase is metastable and was so far only grown and stabilized on cubic substrates, producing nanocrystalline ZnO thin films [20,21]. At extreme pressures, ZnO transforms into the CsCl structure type [22], but efforts to recover it to ambient conditions have failed so far.

Nanocomposites are another class of ZnO materials where individual nanoparticles serve as building blocks [23,24]. To resolve and understand the structures and morphologies of these fundamental units, atomistic simulations such as structural searches have been extensively used in the last decades on ZnO clusters. Already in 1994, Behrman *et al.* [25] studied small ZnO clusters with molecular dynamics simulations, concluding that the ground-state configurations of $(ZnO)_n$ with $n = \{4,6,11,12,15\}$ take the form of cubes, hexagonal prisms, and bubbles. Later studies used density functional theory (DFT) calculations to investigate the shapes and properties of ZnO clusters [26–28], some in conjunction with global optimization methods [29]. Overall, the results agree that a structural crossover from two-dimensional (2D) rings to three-dimensional (3D) cages/tubes occurs at $n = 8$, the origin of which has been extensively discussed in the literature [30]. With increasing computational resources, larger clusters have recently been investigated, both using global geometry optimization methods as well as on hypothetical fullerene structures and clusters cut from bulk [31–34].

Similar theoretical investigations have also been conducted for crystalline ZnO materials in the search for viable polymorphs at ambient conditions [35–37] and at high pressures [38]. Most hypothetical structures proposed in the above studies are, however, strongly metastable, with formation energies significantly higher than both the WZ and ZB structures. Two of the lowest energy polymorphs predicted to date are the body-centered tetragonal (BCT) and the sodalite phases, both of which exhibit a significantly lower density than WZ/ZB [36]. In fact, such low-density materials have many potential applications in the field of energy and sustainability, e.g., in catalysis, for gas separation, for water purification, and for batteries [39]. Furthermore, structures with large voids can easily host guest atoms which can be used to tune the material properties. Recently, several low-density and nanoporous polymorphs of ZnO were reported which could be potentially relevant as materials for band-gap engineering [37,40].

*amsler.max@gmail.com

Despite the extensive work on ZnO materials in the literature, a large part of the configurational space in ZnO still remains unexplored due to the high complexity of its potential energy landscape. In fact, for large clusters $(ZnO)_n$ with $n > 32$ the reported structures and therefore their properties are mostly derived from chemical intuition [41], and only limited studies using a systematic structure search method have been performed [34] due to the high computational cost. To address this issue, in this work we trained a highly transferable, efficient interatomic neural-network potential based on the charge equilibration via a neural-network technique (CENT) [42,43], which allowed us to deal with large systems. Using CENT together with the minima hopping structure prediction method (MHM), we identified a so far unreported putative ground-state structure for $(ZnO)_{32}$. Since experimental mass spectrometric measurements are conducted on ionized clusters [44,45], it is crucial to also study charged clusters $(ZnO)_n^+$ from atomistic simulations. So far, no systematic structural searches have been reported in the literature, to the best of our knowledge, and all studies on $(ZnO)_n^+$ have been carried out starting from structures found in neutral systems. Here we therefore investigated charged $(ZnO)_n^+$ clusters, $n = \{3-10,12\}$ using a structure prediction method and present a list of their putative ground-state geometries.

We also studied the potential of forming crystalline low-density ZnO polymorphs from clusters in a bottom-up fashion. Since many of the clusters $(ZnO)_n$, $n > 8$ exhibit cage- and tubelike geometries, we hypothesize that these structural features of voids would carry on to crystalline solids when assembled from clusters. To predict such structural motifs in ZnO, we explored the potential energy landscape specifically aimed at low-density polymorphs and discovered more than 50 new metastable ZnO phases with low energies. By carefully analyzing their structures, we conclude that many cagelike building blocks are closely linked to the clusters observed in $(ZnO)_n$ and $(ZnO)_n^+$, with sizes $n < 16$.

The manuscript is organization as follows. In Sec. II we describe the methods used in this work. Section III A contains the results on molecular structures of ZnO, whereas Sec. III B summarizes the results on low-density crystalline polymorphs. Our main findings and conclusions are discussed in Sec. IV.

II. METHOD

The potential energy landscape of molecular and crystalline ZnO was explored with the MHM, which implements an efficient structure prediction algorithm [46–49]. Consecutive short molecular dynamics simulations are performed to escape from local minima, followed by local geometry relaxations, taking into account the atomic and, for crystalline structures, cell variables. A combination of the stabilized quasi-Newton minimizer (SQNM) [50], the fast inertial relaxation engine (FIRE) [51], and the Broyden-Fletcher-Goldfarb-Shanno (BFGS) [52,53] algorithm is used for the relaxations. The initial molecular dynamics velocities are approximately aligned along soft mode directions [54] to exploit the Bell-Evans-Polanyi principle [55,56] and accelerate the search. The predictive power of this approach has been demonstrated in a wide range of applications [57–63]. A modified version of the MHM in the MINHOCAO package was used to specifically search for low-density ZnO crystals, where fictitious Lennard-Jones spheres are used to create voids in the system [64].

A prescreening of the energy landscape was performed using empirical and semiempirical methods to model the atomic interactions. On one hand, a density functional tight binding model was used [65] as implemented in the DFTB+ package together with the Slater-Koster parameters for Zn-containing materials [66]. On the other hand, we specifically trained our own artificial neural-network potential for ionic systems based on a charge equilibration scheme (CENT) [42]. Symmetry functions are used as the atomic environment descriptors [67]. The training data was obtained from electronic structure calculations at the DFT level. A dataset containing 8000 $(ZnO)_n$ clusters with sizes ranging from $n = 16$ to 98 was used, resulting in a CENT potential with an accuracy of 8 meV/atom compared to DFT reference data.

Since a large structural diversity in the reference data is crucial to generate accurate potentials based on machine-learning schemes, we took great care in filtering our training database. Data points were split into two groups: training and validation. Training data points were used to fit the neural-network weights during a training process. Separate validation data points were used to evaluate the quality of the potentials in different training runs. Among several fits using various neural-network (NN) architectures and several training runs with different initial random numbers for the NN weights, we selected the best compromise between small rms error and transferability of the potential for training and validation data sets, resulting in the final architecture denoted by 51-3-3-1, i.e., 51 symmetry functions, two hidden layers, each containing three nodes, and the one-node output layer. In order to avoid overfitting, all training runs were performed with only 12 epochs. Although no periodic structures were used for the training process, CENT has proven to be highly transferable for different systems [43]. After verifying that the energetics and geometries of known polymorphs of ZnO were well reproduced, the CENT potential was used as a prescreening tool for both molecular and crystalline systems.

Two different software packages were used for the DFT calculations to refine the CENT and DFTB+ results, and to train CENT. First, we used the *ab initio* molecular simulation package (FHI-AIMS) [68], which employs a numeric atom-centered orbital basis set to generate the training dataset for the CENT potential. The Perdew-Burke-Ernzerhof (PBE) [69] approximation to the exchange-correlation potential was used both for the training dataset of CENT and to evaluate the formation energies. Second, we also used the BIGDFT package, which employs a Daubechies wavelet basis set [70,71], to verify the FHI-AIMS DFT results. The basis functions were placed on a grid with a spacing of 0.3 Å, and the norm conserving GTH-HGH pseudo-potentials [72,73] were used to approximate the core electrons. The final geometries were relaxed until the maximum force component was less than 10 meV/Å.

Since semilocal functionals are well known to systematically underestimate the band gaps, the hybrid PBE0 [74,75] and B3LYP [76] functionals were used on top of the PBE relaxed geometries to obtain the electronic properties. Additionally, the band gaps were computed with PBE0 for selected crystalline structures. The band-gap errors compared to PBE

were found to lie consistently within 2.30 ± 0.01 eV, such that a scissor operator was subsequently used to obtain corrected band gaps where a rigid shift of 2.30 eV was applied to the conduction bands.

To evaluate the dynamical stability of the crystalline structures, phonon calculations were carried out with the frozen phonon approach as implemented in the PHONOPY package [77]. Depending on the unit-cell size, supercells of dimensions up to $4 \times 4 \times 4$ were used. For large unit cells, the supercell dimensions were reduced to lower the computational cost.

III. RESULTS AND DISCUSSION

A. Clusters

1. Neutral

We performed MHM calculations using the CENT potential for neutral $(ZnO)_n$ clusters with $n = \{12,16,24,32,36\}$, starting from random seed structures. We chose these medium-sized systems because they have been extensively studied in the past and provide a benchmark system for our methods. Our results for the $(ZnO)_n$ clusters with $n = \{12,16,24\}$ are in good agreement with the findings of Al-Sunaidi *et al.* [41], who used an evolutionary structure prediction algorithm, while for $n = 36$ our results agree with the reports of Wang *et al.* [31]. In contrast to $(ZnO)_n$ clusters with $n < 12$, where the ground-state structures have ringlike structural motifs, the larger clusters with $n = 12,16,24$ form perfectly closed cages, which only contain hexagons and tetragons. In fact, even larger clusters are expected to form so-called "open cages" containing octagons. The detailed results for each structure size are discussed below.

Figure 1 shows the three lowest energy structures for $(ZnO)_{12}$, $(ZnO)_{16}$, and $(ZnO)_{24}$, where the labels (i), (ii), and (iii) denote the energetic ordering. The global minimum (GM) configuration of $(ZnO)_{12}$ is a sodalite cage with T_h symmetry, consisting of eight hexagons and six tetragons. Similarly, the GM of $(ZnO)_{16}$ is a sodalite cage as well, with T_d symmetry (spheroid cage), consisting of 12 hexagons and six tetragons. In fact, these clusters are the main building block for the crystalline sodalite structures (SOD and SOD-cub) [78,79]. The most stable structure of $(ZnO)_{24}$ is a tubelike structure with S_8 symmetry, consisting of two octagons, eight squares, and 16 hexagons.

For these three systems, $n = 12,16,24$, the structures of the GM configuration are in agreement with earlier theoretical results [25,41]. The stability of these cages can be compared based on the energy differences between the GM and the second lowest energy configuration, which are 1.242, 0.177, and 0.316 eV for $(ZnO)_{12}$, $(ZnO)_{16}$, and $(ZnO)_{24}$, respectively. For $(ZnO)_{12}$, the energy difference between (ii) and GM is 1 order of magnitude higher than for $n = 16$ and 24, which agrees well with the results in the literature [30,41]. Due to its high stability, $(ZnO)_{12}$ is also referred to as a "magic" cluster [34], where the GM is fully trigonally coordinated but the second lowest energy structure [12 (ii)] is not. The second lowest energy structure of $(ZnO)_{12}$ and $(ZnO)_{24}$ clusters are both distorted cages consisting primarily of squares, hexagons and octagons. The second and third lowest energy structure of the $(ZnO)_{16}$ cluster are cages with C_{3v} and S_8 symmetry, respectively.

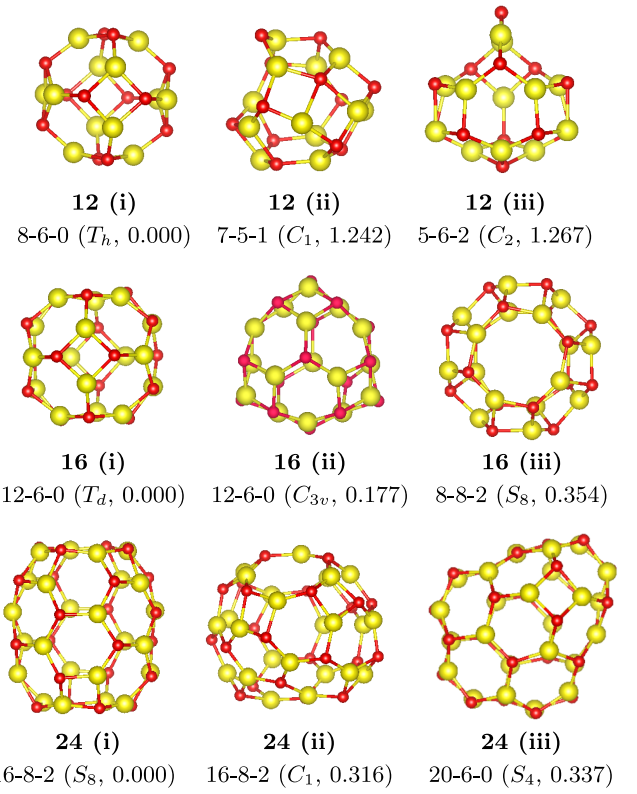

FIG. 1. Lowest energy and metastable structures of $(ZnO)_{12}$, $(ZnO)_{16}$, and $(ZnO)_{24}$. The labels i-j-k indicate the number of hexagons, tetragons, and octagons, respectively. The values in parentheses represent the symmetries and relative energies of the configurations in electronvolts, respectively. Yellow (large) and red (small) spheres denote Zn and O atoms, respectively.

All results presented so far validate earlier studies, and the success in recovering previously reported low-energy structures demonstrates that both the CENT potential and the MHM produce results with reliable accuracy. For the $(ZnO)_{32}$ cluster, however, we found a new high-symmetry structure as the lowest energy configuration, illustrating the predictive power of our approach. As shown in panel (i) of Fig. 2, the GM is a tubelike structure with S_8 symmetry, consisting of 24 hexagonal, eight tetragonal, and two octagonal faces. The first metastable phase, shown in panel (ii), is a nested cage $(ZnO)_4@(ZnO)_{28}$ with T symmetry, which was recently predicted by Chen *et al.* [34]. A similar nested cage configuration $[(ZnO)_6@(ZnO)_{28}]$ for $(ZnO)_{34}$ has been proposed as the putative ground state by Dmytruk *et al.* [80]. On the other hand, Wang *et al.* [81] predicted closed-cage structures irrespective of the cluster size, resembling our putative ground state for $(ZnO)_{32}$. These contradictory results indicate that structure prediction strongly depends on the employed computational framework, and a thorough exploration of the energy landscape using complementing methods is called for to validate computational predictions.

2. Ionized

Motivated by the success of our approach on neutral clusters, we decided to apply our method on ionized systems

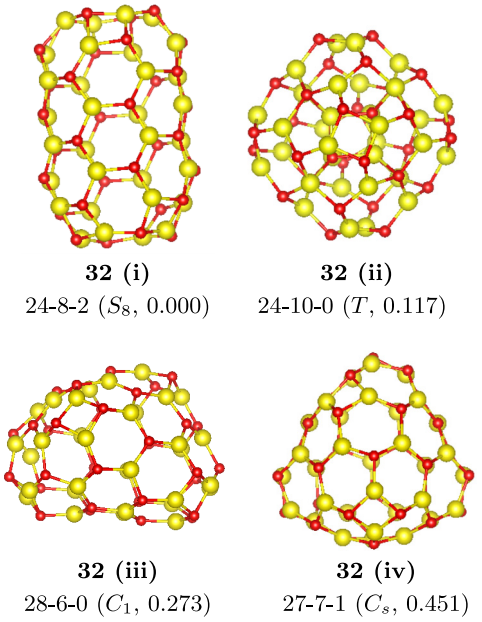

FIG. 2. Lowest energy and metastable structures of $(ZnO)_{32}$. The labels i-j-k indicate the number of hexagons, tetragons, and octagons, respectively. The values in parentheses represent the symmetries and relative energies of the configurations in electronvolts, respectively. Yellow (large) and red (small) spheres denote Zn and O atoms, respectively.

which have not yet been thoroughly explored in the past. Experimental mass spectrometric measurements are in general performed on ionized clusters [44,45], but most theoretical studies only consider neutral systems due to the reduced computational cost. In fact, the study of charged clusters is also of importance in solids. When, for example, zinc oxide clusters are introduced into zeolite frameworks, they become positively charged, which causes a change in their structures [82]. The limited amount of studies on ionized clusters so far used input geometries from neutral clusters and reranked them according to their energies after removing one electron [28,83], and no systematic structure prediction calculations have been reported in the literature.

We thus carried out a global structure optimization with the MHM for small charged clusters $(ZnO)_n^+$ with $n = \{3-10,12\}$. According to our results, the structures and relative stabilities of the ionized $(ZnO)_n^+$ clusters differ significantly from the neutral ones in several systems. To verify the energetic ordering of the charged clusters and to compare with earlier results in the literature, we also computed the contribution of the vibrational zero point energy (ZPE). Although including the ZPE does influence the values of the energy differences, the energetic ordering was never changed in any of the systems studied here. Below we discuss the differences between the neutral and ionized systems for every cluster size separately, taking also into account the earlier predictions on the charged clusters in Refs. [44] and [83]. The lowest energy structures are shown in Figs. 3 and 4 for $n = \{3-8\}$ and $n = 9,10,12$, respectively.

For the smallest cluster size $(ZnO)_3^+$, the three lowest energy structures agree overall with the ones in the neutral system [29]. However, structures (ii) and (iii) differ from their neutral counterparts in that they are completely planar when ionized.

TABLE I. Relative energies, in electronvolts, of the three lowest energy configurations of $(ZnO)_6^+$, calculated with the conventional PBE exchange-correlation functional using two different codes as well as a with the hybrid B3LYP functional. Whenever indicated, the ZPE was taken into account.

Method	**6(i)**	**6(ii)**	**6(iii)**
PBE (BIGDFT)	0.0	0.977	1.073
PBE (FHI-AIMS)	0.0	1.089	1.277
PBE+ZPE (FHI-AIMS)	0.0	1.050	1.236
B3LYP (FHI-AIMS)	0.0	1.130	1.433
previous results (B3LYP+ZPE) [44]	0.0	0.670	0.280

The change from buckled to planar geometry after ionization was also reported in Ref. [44] but with a reversed energetic ordering of the zigzag and the 2D structure.

For $(ZnO)_4^+$ and $(ZnO)_5^+$, our predictions are in excellent agreement with the results of Koyasu *et al.* [44], and the energetic ordering of the neutral and ionized clusters are identical [29,34].

For the $(ZnO)_6^+$ clusters, the three lowest energy configurations found during our structural search agree with the ones reported in the literature [44]. However, the energetic ordering differs significantly. Although our results agree on the GM structure, the ordering of the two first metastable isomers is reversed. For this system, we list the energies of the three lowest $(ZnO)_6^+$ isomers in Table I using different functionals and codes, together with the results of Koyasu *et al.*, who employed DFT calculations with the hybrid B3LYP functional [44]. Independent of the method, we consistently get the same result that the tricyclic structure is lower in energy than the tube structure.

The geometries of the GM and (ii) in $(ZnO)_7^+$ agree with the neutral system [29]. Our results also agree with Koyasu *et al.* for the two lowest energy structures. But similar to $(ZnO)_6^+$, the next lowest isomer is predict to be a tube structure by Koyasu *et al.* In contrast, we find a tetracyclic structure to be the third lowest energy structure (iii), as shown in Fig. 3, which is ranked number 8 in the neutral system (7i in Fig. 1 of Ref. [29]).

For the $(ZnO)_8^+$ cation the geometries of the three lowest isomers agree overall with the results of Koyasu *et al.*, but the energetic ordering completely differs from our results (see lowest panels in Fig. 3). Koyasu *et al.* predicted that the GM has a tubelike geometry, while our calculations show that the tricyclic isomer is favored. This isomer is the GM also in the neutral systems [29]. Surprisingly, the cyclic structure (ii), which is 0.473 eV above the tricyclic GM in $(ZnO)_8$ [29], is merely 0.026 eV above the GM in our calculations and therefore almost degenerate in energy. Hence, the cyclic structure could be found as a metastable cluster in experiments.

For $(ZnO)_9^+$, our predicted GM configuration differs from the one reported in Ref. [83]. A comparison with the results of Sunaidi *et al.* [41] shows that the GM, however, has the same geometry as a highly metastable cluster of neutral $(ZnO)_9$, which they refer to as 9 (g) (Fig. 5 of Ref. [41]). On the other hand, the putative ground-state structure of neutral $(ZnO)_9$ is only the third-lowest structure for $(ZnO)_9^+$ cations, denoted as 9 (iii) in Fig. 4.

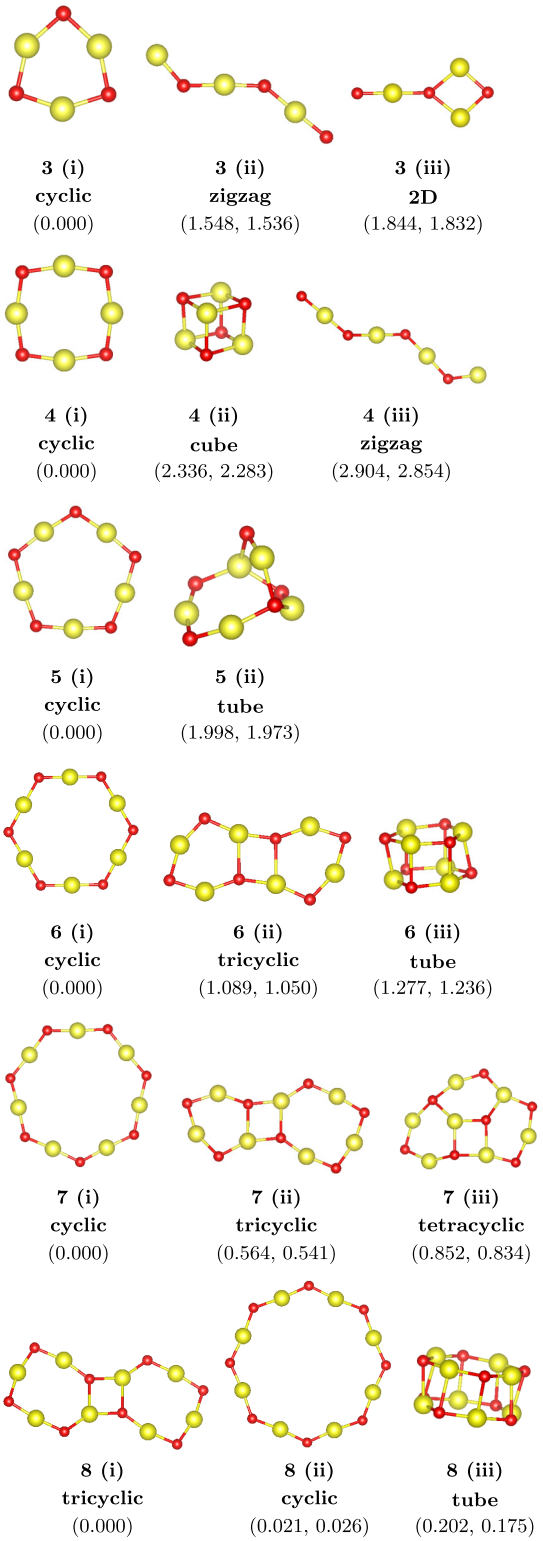

FIG. 3. Lowest energy and metastable structures of $(ZnO)_6^+$ and $(ZnO)_8^+$. Values in parentheses represent relative energies with respect to the GM in electronvolts, without and with taking into account the ZPE, respectively. Yellow (large) and red (small) spheres denote Zn and O atoms, respectively.

Since no theoretical predicted structures have been so far reported in the literature for systems with $n = 10,12$, we compared our structures solely with the putative GM of

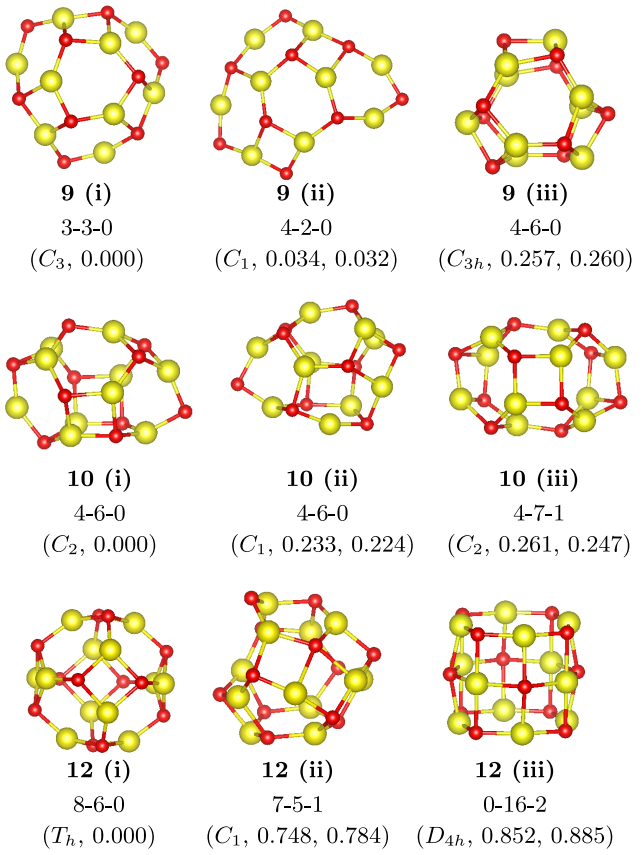

FIG. 4. Lowest energy and metastable structures of $(ZnO)_9^+$, $(ZnO)_{10}^+$, and $(ZnO)_{12}^+$. The labels i-j-k indicate the number of hexagons, tetragons, and octagons, respectively. Values in parentheses represent relative energies with respect to the GM in electronvolts, without and with taking into account the ZPE, respectively. Yellow (large) and red (small) spheres denote Zn and O atoms, respectively.

neutral clusters of identical size. The GM for $(ZnO)_{10}^+$ does not appear in the list of the ten lowest structures in the work of Sunaidi *et al.* [41] nor in Ref. [29], and we thus expect that it is completely new. The GM of the neutral system was found to be the third lowest structure, denoted as 10 (iii) in Fig. 4, corresponding to structure 10 (A) in Fig. 6 of Ref. [41].

Finally, for the $(ZnO)_{12}^+$ clusters the two lowest isomers are geometrically identical to the their neutral counterparts, as a comparison with Fig. 1 clearly shows, which is not surprising given the high stability of the GM of $(ZnO)_{12}$. Note that the relative stability of the GM compared to the first metastable configuration is, however, significantly smaller than in the neutral system. This destabilization as a consequence of the reduced energy difference can be attributed to a delocalization of the unpaired electron over oxygen atoms for the ionized cluster. The third lowest structure is different from the neutral counterpart, for which we predict a tube structure.

Overall, our comparison between the neutral and ionized clusters shows that the ordering of the lowest energy structures can change significantly for some cluster sizes. The general trend of ring-shaped GM structures for $n = 1$–8 persists in

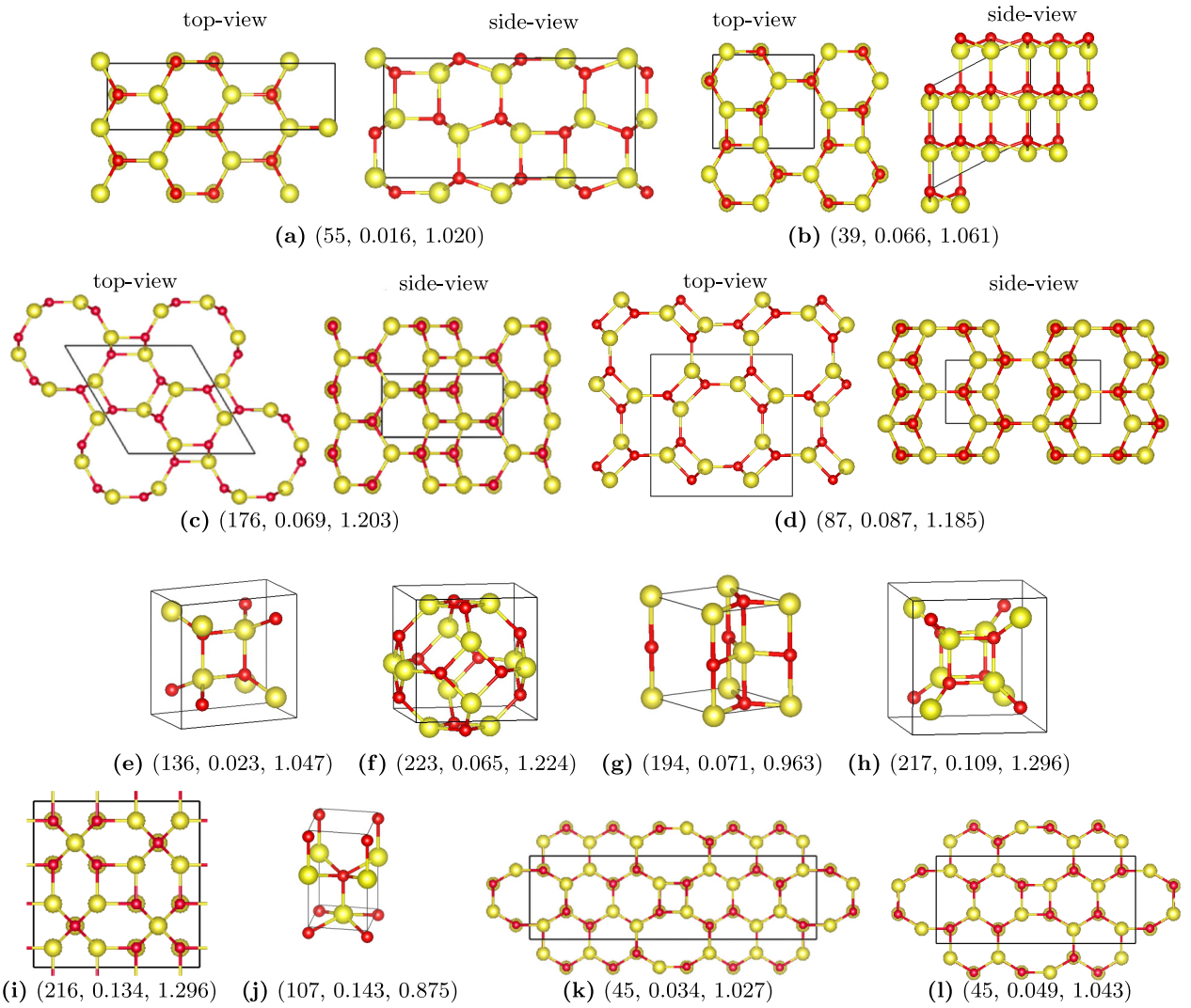

FIG. 5. Structures reported in the literature with their space groups, relative energies in eV/atom, and relative atomic volumes (V/V_{WZ}): (a) $59-4-280312$ type [37]; (b) ATV type [37]; (c) CAN type [40]; (d) ATN type [37]; (e) BCT type [86]; (f) SOD type [37,86]; (g) graphitic or h-BN type [38]; (h) cubane type [38]; (i) SOD-cub type [87]; (j) GeP type [38]; and (k) and (l) are two different polymorphs of MgO type and are five-coordinated [87]. The black boxes denote the unit cells.

both $(ZnO)_n^+$ and $(ZnO)_n$. However, the ordering of the next higher energy configurations differ even with respect to the results in the literature [44,83]. Furthermore, the well-studied crossover between ring or planar 2D structures to 3D structural motifs in neutral clusters at $n = 8$ appears to occur at a larger size in ionized clusters. Even at $n = 9$, the GM and first excited states are slightly curved, almost flat flakes. The first truly 3D cagelike GM structure is found in $(ZnO)_{10}^+$.

B. Crystals

Crystalline structures were explored with the fully periodic version of the MHM. Initially, two complementary methods were used to prescreen the potential energy landscape. First, we performed a search specifically for low-density polymorphs by using a modified MHM approach with fictitious Lennard-Jones (LJ) spheres to create internal pressure and voids in the system. These LJ atoms were then removed from the system, similar to the chemical degassing process used in clathrate materials to get rid of guest atoms in the cage structures [64,84,85]. Different stoichiometries $(ZnO)_xLJ_y$ were studied, where x and y were chosen in the range of $x = 8$–18 and $y = 0$–3. Specifically, the following stoichiometries were used: $(ZnO)_8LJ_0$, $(ZnO)_8LJ_1$, $(ZnO)_8LJ_2$, $(ZnO)_{10}LJ_2$, $(ZnO)_{12}LJ_1$, $(ZnO)_{12}LJ_2$, $(ZnO)_{14}LJ_2$, $(ZnO)_{16}LJ_2$, and $(ZnO)_{18}LJ_3$. Second, we employed the same CENT potential as used for the search of new molecular structures, at the stoichiometries $(ZnO)_{10}$, $(ZnO)_{12}$, $(ZnO)_{14}$, $(ZnO)_{16}$, and $(ZnO)_{18}$. An alternate approach was used to generate low-density polymorphs, namely, by performing the structural searches at negative pressure in the range of 0.1–1.0 GPa.

At least two different MHM runs were performed for each composition, starting from random initial configurations, scanning several thousand distinct local minima. Before refining the results at the DFT level, we carefully filtered this large amount of data with respect to three criteria. First, we employed an energy threshold to eliminate all candidate structures that are higher in energy than 300 meV/atom

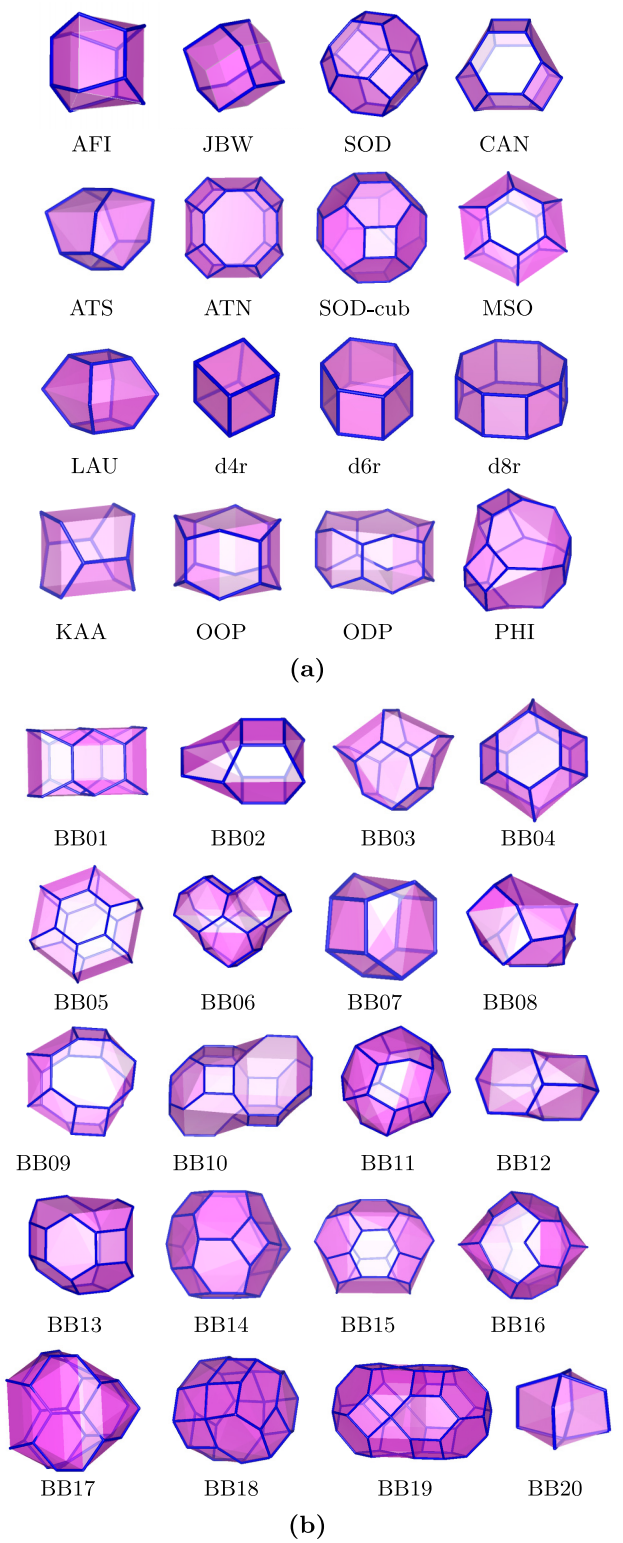

FIG. 6. Examples of (a) building blocks for zeolite frameworks and (b) new building blocks encountered in the new low-density polymorphs.

above the WZ ground-state structure. Second, we eliminated low-symmetry candidates, since many of them are essentially defect structures of perfectly crystalline materials. Finally, structure prediction calculations can result in many duplicates, which were eliminated by comparing the structures based on fingerprint distances using the Gaussian overlap method [88]. Based on these filters, a total of 300 candidate structures were used as starting points of local relaxations using DFT. In total, 57 novel polymorphs were identified, and their structural features are discussed in the following section.

1. *Structures and properties of ZnO polymorphs*

During the structural search we recovered a range of phases already reported in the literature, a strong indication that the MHM simulations were well converged. Besides the well-known polymorphs like the WZ and ZB structure, also the BCT [18,86] and the sodalite phases [86,87] were found, together with many of their stacking variants, so-called polytypes [89,90]. Similar structures have been reported in other binary compounds such as MgO and ZnS systems [87,91,92]. Furthermore, we discovered a range of low-density polymorphs, such as zeolite frameworks. Many of the previously reported structures in Refs. [37] and [38] were also found, for example, the 59-4-280312 structure with $P2_1/b2_1/a2/m$ symmetry [37], which is in fact a binary version of Z-carbon [58] and merely 16.4 meV/atom higher in energy than WZ according to our calculations. The structures of all these polymorphs are shown in Fig. 5 together with their relative atomic volumes and relative atomic energies. Additionally, we screened the IZA Database of Zeolite Structures [93] to identify previously reported phases.

Besides all these known polymorphs of ZnO we discovered a plethora of novel low-density structures with three-, four-, five-, or six-coordinated atoms. Structural motifs leading to the low density are diverse, ranging from wide one-dimensional channels which either run in one, two, or three dimensions, can be straight, or even run in zigzag lines through the material, and zero-dimensional cages. In fact, some of these zero-dimensional cages are fundamental building blocks which are strongly related to stable and metastable hollow $(ZnO)_n$ clusters. Especially the magic clusters with high symmetry often serve as building blocks in low-density polymorphs such as CAN $[(ZnO)_9]$, SOD $[(ZnO)_{12}]$, and SOD-cub $[(ZnO)_{16}]$. The occurrence of these magic clusters as building blocks has been exploited in previous studies to construct hypothetical crystal structures in a bottom-up approach [94,95], which were also recovered during our structural search. However, our unconstrained approach uncovered many more potential building blocks that had not been considered before. In Fig. 6 all zero-dimensional building blocks encountered in the novel ZnO phases are listed. The top part (a) contains well-known zeolite structures of cations surrounded by four oxygen anions, labeled accordingly [82]. The bottom set of building blocks in (b) are new, enumerated with labels from BB01 to BB20. To show which of these building blocks have been predicted as low-energy structures in clusters, we compiled a list of several building blocks in Table II together with their corresponding clusters, labeled according to the convention in Ref. [41]. Figure 7 shows the structures of the 22 new lowest energy low-density ZnO polymorphs. The polyhedra represent the cagelike building blocks, which are individually listed in Fig. 6. For each of the structures, the corresponding space-group numbers, relative energies, and volumes (V/V_{WZ}) with respect to the

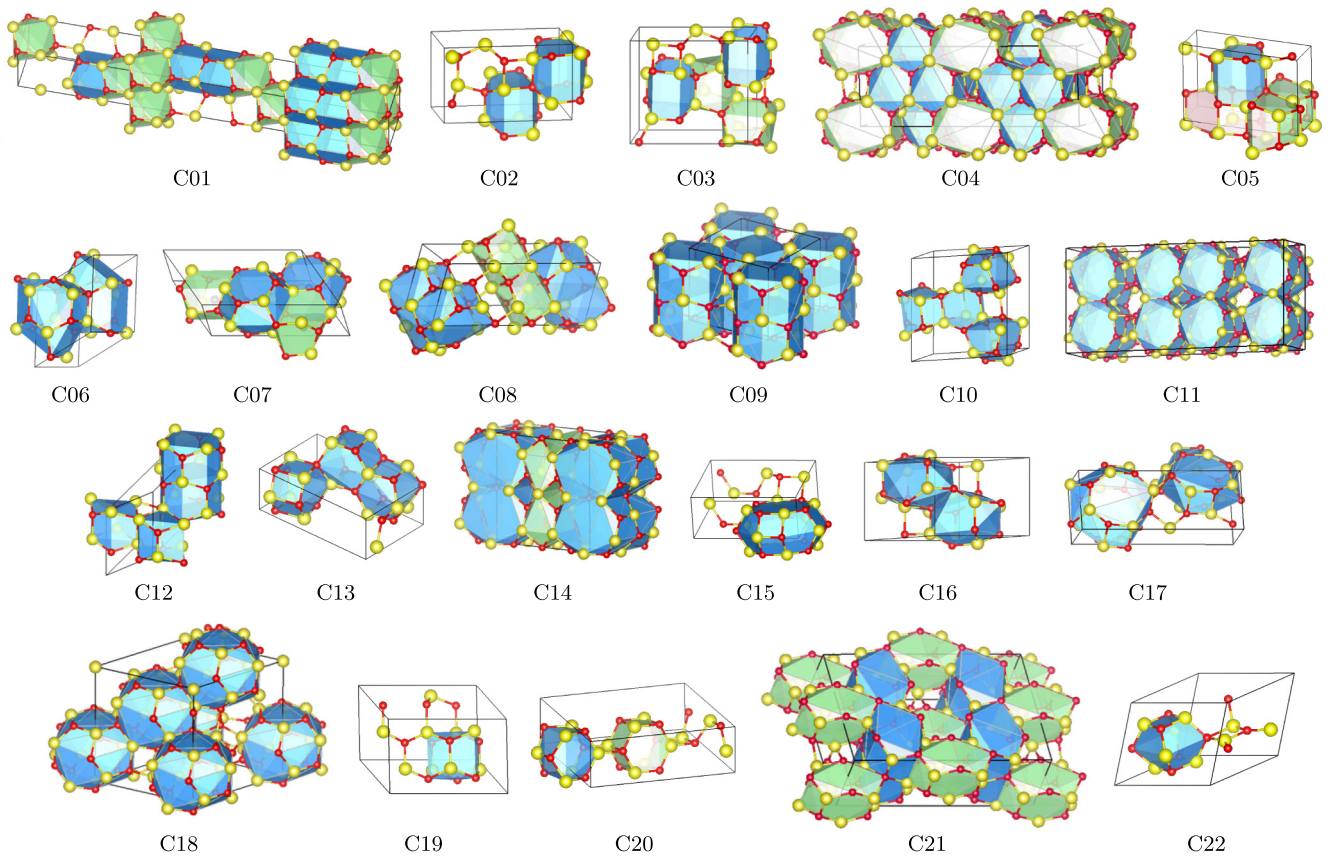

FIG. 7. The 22 new low-energy, low-density phases of ZnO, enumerated from C01 to C22. The cagelike building blocks are represented with polyhedra, which are shown individually in Fig. 6. Yellow (large) and red (small) spheres denote Zn and O atoms, respectively.

ground-state Wurtzite structure are listed in Table III. This data is also presented in a scatter plot in Fig. 8, showing not only that almost all structures have lower density than WZ, but also that many phases have volumes/atom even exceeding a factor of 1.2 with respect to WZ. Table III also lists the

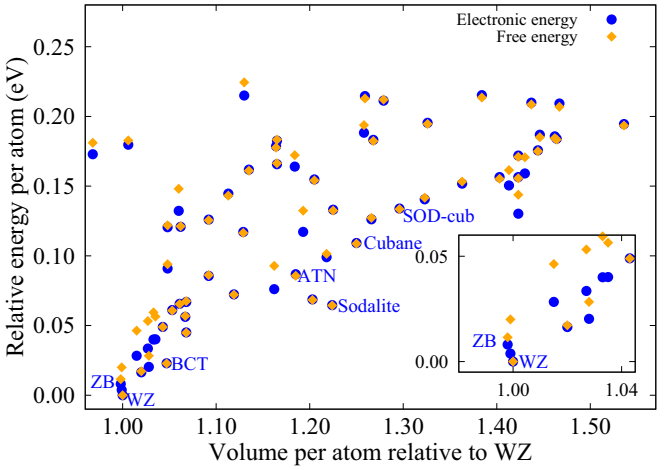

FIG. 8. Potential (circles) and free energies (squares) at 300 K with respect to the wurtzite phase of all studied structures plotted against relative volume (V/V_{WZ}). The inset shows the energies of polymorphs close to the WZ phase with respect to their energies and densities.

elemental building blocks in the structures. For example, the first structure in the list "C01" is composed of only the AFI and JBW zeolite frameworks, which on their own are the elemental building blocks of WZ and ZB, respectively. It is thus not surprising that "C01" lies energetically between WZ and ZB. This particular polytype has not been reported in the literature before and has a relative energy of merely 3.8 meV/atom and $R\bar{3}m$ symmetry, and the phonon calculations show that this phase is also dynamically stable at ambient conditions (Fig. 9). In fact, the phonon dispersion of each of the novel phases was computed using PHONOPY [77] to ensure dynamical stability. No imaginary modes were observed (see Supplemental Materials [96]), indicating that all structures are metastable. Very few structures exhibit slightly imaginary acoustic modes near the Γ point, which we, however, attribute to numerical noise in the forces arising from the discrete real space grid employed in FHI-AIMS [97].

We also reinvestigated the graphitic phase of ZnO, which was predicted through *ab initio* calculations [18,86,98,99] and subsequently experimentally observed as thin films on a substrate [100]. It is well known that only a few layers of this 2D material are viable. However, this polymorph has been studied extensively in its bulk phase. Our phonon calculations reveal that graphitic ZnO exhibits imaginary phonons, indicating that it is in fact dynamically unstable. A local relaxation with a very tight convergence criterion indeed leads to buckling of the sheets and its transformation to the

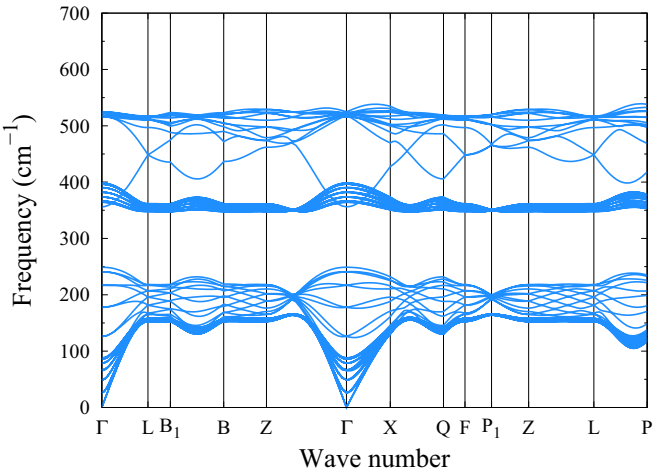

FIG. 9. PBE phonon dispersion for C01. Note that the LO-TO splitting was neglected.

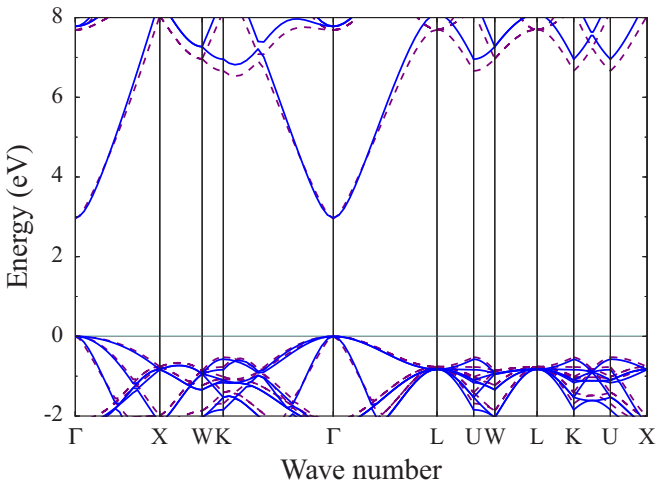

FIG. 10. Comparison of the shifted PBE (dashed lines) and the PBE0 electronic band structure (solid lines) for ZB ZnO. The Fermi level is denoted by the horizontal line.

WZ structure. These findings support the experimental reports that only a few monolayers of graphitic ZnO are stable.

With the phonon calculations at hand, we computed the free energies within the harmonic approximation to evaluate the influence of the vibrational entropy on the phase stabilities. The free energy differences with respect to WZ at 300 K are plotted in Fig. 8 as yellow squares. For most phases, the vibrational contribution to the free energy only slightly affects the stability. However, the energetic ordering of some of the lowest energy polymorphs with higher density changes significantly. For example, the new C01 structure, which is energetically lower than ZB, has a higher free energy than ZB at elevated temperatures (see inset of Fig. 8). Nevertheless, this phase could be synthesized at low temperatures or through epitaxial growth on an appropriate substrate.

TABLE II. Relation between several of the building blocks shown in Fig. 6 and cagelike structures observed in ZnO clusters. The building blocks were isolated from the bulk crystals and relaxed in vacuum before comparing to the reference cluster structures. The structure designations from previous studies are listed in the second column, while the third column lists the labels used in Sec. III A of the current work whenever available.

Building block	Ref. [41] cluster	Current cluster
SOD	12(A)	$(ZnO)_{12}$/$(ZnO)^{+}_{12}$ (i)
CAN	9(A)	$(ZnO)^{+}_{9}$ (iii)
SOD-cub	16(A)	$(ZnO)_{16}$ (i)
d4r	4(B)	$(ZnO)^{+}_{4}$ (ii)
d6r	6(A)	$(ZnO)^{+}_{6}$ (iii)
d8r	8(B)	$(ZnO)^{+}_{8}$ (iii)
KKA	6(A)	$(ZnO)^{+}_{6}$ (iii)
OOP	8(B)	$(ZnO)^{+}_{8}$ (iii)
ODP	10(N)	
PHI	12(H)	
BB01	10(C)	
BB03	9(A)	$(ZnO)^{+}_{9}$ (iii)
BB04	9(B)	
BB07	6(B)	
BB14	16(B)	$(ZnO)_{16}$ (ii)
BB15	15(A)	
BB18	16(B)	$(ZnO)_{16}$ (ii)

The electronic band structures and gaps were not directly computed with the PBE exchange-correlation functional. Semilocal functionals such as PBE are well known to underestimate the band gaps. Hybrid functionals like PBE0, on the other hand, give more accurate results, but at a significantly higher computational cost. Table IV summarizes the PBE/PBE0 results for several ZnO polymorphs (wurtzite, zinc-blende, sodalite, and BCT types), which are in good agreement with previous experimental [101,102] and theoretical [86] studies. Based on this data and the PBE/PBE0 results of several other ZnO polymorphs, we find that the PBE0 band gaps are on average 2.30 ± 0.01 eV larger than with PBE. This rigid shift can be also applied to the complete band structure, as shown in Fig. 10 for ZB, where both the valence and conduction bands of PBE0 are well reproduced by the shifted PBE bands. Therefore, the reported gaps in Table III are based on shifted PBE calculations. Figure 11 shows the shifted band structure of WZ, ZB, and the new C01 polytype. C01 is a direct semiconductor with a gap of 2.99 eV, a value exactly between WZ and ZB. All other band structures of the new polymorphs are included in the Supplemental Materials [96].

An analysis of the volumes and the band gaps in Table III reveals that larger gaps are often observed in polymorphs with larger volumes. However, our data shows only a weak correlation with $R^2 = 0.262$. A similar effect had been found by Demiroglu *et al.* [40], who analyzed a dataset of four-coordinated low-density polymorphs of ZnO with varying pore sizes and observed a strong correlation of the band gaps and the valence band maxima with pore volumes. In contrast to Demiroglu's dataset, which mainly contains four-coordinated ions with similar local structural environments, our structures are more diverse. This difference in the structural motifs of the configurations can readily explain the observed discrepancy in the magnitude of the correlation.

TABLE III. Structural data of the new low-density ZnO phases. Column 1 contains our structural label, followed by the space group in the Hermann-Mauguin notation. Column 3 contains the characterization of the building blocks. Columns 4, 5, and 6 contain the energy per atom and the free energy per atom at 300 K with respect to WZ and the relative volume per atom, respectively. Column 7 contains the shifted PBE band gap. In the last column we list the coordination of Zn atoms found in the structures.

Label	Space group	Building blocks	Energy (eV)	Free energy (eV)	Vol/Vol$_{WZ}$	Gap (eV)	Coord.
C01	$R\bar{3}m$ (160)	AFI, JBW	0.004	0.020	0.999	2.99	4
C02	$Cmc2_1$ (36)	KAA	0.020	0.028	1.028	3.05	4
C03	$Imm2$ (44)	AFI, KAA	0.028	0.046	1.015	3.03	4
C04	$Aem2$ (39)	AFI, OOP	0.040	0.059	1.033	3.11	4
C05	$C2/m$ (12)	ATS,KAA,BB02	0.040	0.056	1.035	3.08	4
C06	$Cmc2_1$ (36)	BB03	0.045	0.045	1.068	3.14	4
C07	$Cmcm$ (63)	BB04, AFI	0.056	0.057	1.067	3.17	4
C08	$Pmn2_1$ (31)	BB06, JBW	0.067	0.068	1.068	3.03	4
C09	$I4cm$ (108)	OOP	0.072	0.072	1.119	3.24	4
C10	$Immm$ (71)	ATS	0.076	0.093	1.162	3.03	4
C11	$Fmm2$ (42)	OOP	0.086	0.086	1.092	3.06	4
C12	$Fmm2$ (42)	AFI	0.091	0.094	1.048	3.16	4, 5
C13	$I4/m$ (87)	BB07	0.099	0.101	1.218	3.29	4
C14	$Amm2$ (38)	JBW, ODP	0.117	0.116	1.129	3.15	3, 4, 5
C15	$C2/m$ (12)	ATN	0.117	0.132	1.193	3.32	4
C16	Pc (7)	BB08	0.121	0.122	1.048	3.02	4
C17	$P2_1$ (4)	BB09	0.121	0.121	1.062	3.11	4
C18	$R3$ (146)	BB11	0.126	0.126	1.092	3.08	4
C19	$Aem2$ (39)	JBW	0.126	0.127	1.266	3.22	3, 4
C20	Cm (8)	ATS, d6r	0.130	0.144	1.423	3.43	3, 4
C21	$Fmm2$ (42)	OOP	0.132	0.148	1.060	2.84	4
C22	Cm (8)	LAU	0.133	0.133	1.225	3.15	3, 4
C23	$Pmmm$ (47)	LAU	0.145	0.143	1.113	2.38	4
C24	$P6_3mc$ (186)	SOD	0.151	0.162	1.413	3.60	3, 4
C25	Pm (6)	MSO	0.151	0.150	0.956	2.58	4
C26	$R\bar{3}m$ (160)	SOD,BB13	0.152	0.153	1.363	2.96	3, 4
C27	$I4/mcm$ (140)	d8r	0.153	0.160	0.941	2.96	5, 6
C28	Cm (8)	SOD	0.155	0.154	1.205	3.06	3, 4, 5
C29	Cm (8)	JBW, chain	0.157	0.155	1.403	3.15	3, 4
C30	$Pmc2_1$ (26)	BB15	0.157	0.156	1.423	3.64	3, 4
C31	$P3m1$ (156)	BB10	0.159	0.171	1.430	3.62	3, 4
C32	$Pmc2_1$ (25)	BB18	0.162	0.161	1.135	3.13	4
C33	$I4cm$ (108)	chain	0.162	0.165	1.720	3.49	3, 4
C34	$Pmc2_1$ (25)	chain	0.163	0.162	1.643	3.43	3, 4
C35	Cm (8)	BB04, BB06	0.164	0.172	1.184	2.55	3, 4, 5
C36	$C2/m$ (12)	d6r, d10r	0.165	0.173	0.952	2.78	5, 6
C37	Cm (8)	BB16	0.166	0.166	1.165	2.74	3, 4
C38	Pc (7)	chain	0.172	0.171	1.423	3.34	3, 4
C39	$C2/m$ (12)	d4r, d8r	0.173	0.181	0.968	2.97	5, 6
C40	$C2$ (5)	chain	0.176	0.174	1.963	3.55	3, 4
C41	$Ima2$ (46)	d16r	0.176	0.175	1.444	3.38	3, 4
C42	$I\bar{4}m2$ (119)	BB17	0.179	0.178	1.164	2.99	3, 4
C43	$Fmmm$ (69)	d8r	0.180	0.183	1.006	2.94	5
C44	Cc (9)	BB18	0.183	0.183	1.165	3.21	4, 5
C45	$Imm2$ (44)	BB19	0.183	0.182	1.268	2.78	4
C46	$P2_1$ (4)	chain	0.184	0.183	1.464	3.28	3, 4
C47	Cc (9)	chain	0.186	0.184	1.462	3.40	3, 4
C48	Cm (8)	chain	0.187	0.185	1.446	3.24	2, 3, 4, 5
C49	$I4mm$ (107)	BB20	0.188	0.194	1.258	3.37	4, 5
C50	$P2_1$ (4)	chain	0.195	0.194	1.536	3.52	3, 4
C51	Cc (9)	chain	0.195	0.195	1.326	3.43	3, 4
C52	$Amm2$ (38)	BB12	0.209	0.207	1.467	3.24	3, 4
C53	$P2_1$ (4)	chain	0.210	0.209	1.437	3.46	3, 4
C54	Cm (8)	BB14	0.211	0.212	1.279	3.12	4
C55	$Pmc2_1$ (25)	BB04	0.215	0.213	1.259	2.43	3, 4, 5
C56	$Ibam$ (72)	d4r, d12r	0.215	0.224	1.130	3.00	5
C57	$Imm2$ (44)	d4r	0.215	0.214	1.384	3.08	3, 4, 5

TABLE IV. The band-gap values of well-known ZnO bulk phases evaluated at the PBE and PBE0 levels. Measured band gaps are provided for comparison.

Type	Present		Previous[a]			Expt.
	PBE	PBE0	PBE	HSE	G_0W_0	
Wurtzite	0.74	3.09	0.73	2.25	3.31	3.44[b]
Zinc blende	0.65	2.97	0.63	2.13	3.18	3.27[c]
Ideal BCT	0.76	3.10	0.75	2.26	3.41	
Sodalite	1.06	3.41	1.05	2.43	3.63	
Cubane	1.34	3.63	1.33	2.73	4.00	

[a]Reference [86].
[b]Transmission spectroscopy, Ref. [101].
[c]Reference [102].

We also investigated the influence of different Zn coordinations on the thermodynamic stability and electronic structure of the low-density polymorphs. The last column in Table III contains the coordination numbers observed in each structure. To support our analysis, we visualized this data in Fig. 12, where the top panel shows the energy difference with respect to the ground state and the band gaps, and the lower panel shows a normalized histogram of the Zn coordination numbers. The first striking trend that we notice in Fig. 12 is that the lowest energy phases from C01 up to C11 contain only fourfold-coordinated atoms, and at the same time the band gaps fluctuate very little and lie consistently around a value of slightly above 3 eV. This behavior is not surprising since bonding angles close to the ideal tetrahedral geometry impose minimal structural strain. Also, the small fluctuations in the gap energies agree with the weak correlation of the gaps with respect to changes in volume that we found earlier. For higher energy structures, however, small fractions of three-, five-, and even six-coordinated Zn start to emerge. At the same time, the band gaps begin to fluctuate strongly, reaching values as low as 2.38 and 2.43 eV for C23 and C55, respectively, and as high as 3.64 eV for C30. Surprisingly, while the C23 phase is composed of purely four-coordinated atoms, both C30 and C55 contain fractions of three-coordinated and even five-coordinated atoms. For structures with high energies, the fraction of four-coordinated atoms decreases overall, e.g., the two phases C43 and C56 purely contain five-coordinated atoms in square pyramidal and trigonal bipyramidal geometries. This trend shows that, although tetrahedral geometries are overall favored energetically, a controlled tuning of the coordination geometries in metastable phases could be used to engineer the electronic structure of low-density ZnO materials.

IV. CONCLUSION

In summary, we carried out an extensive search for ZnO nanoclusters and low-density crystalline structures with the minima hopping structure prediction method. A new CENT potential was specifically trained for this task to prescreen the potential energy landscape at a fraction of the computational cost compared to *ab initio* methods. The final results were refined at higher accuracy using different flavors of DFT, leading to the reliable prediction of several new forms of ZnO. For the $(ZnO)_{32}$ clusters we discovered a so far unreported putative ground-state structure with a tubelike geometry. For small ionized ZnO clusters we performed structural searches for $(ZnO)_n^+$ with $n = \{3-10, 12\}$. Our results indicate that considerable differences in geometry and energetic ordering emerge between neutral and ionized ZnO clusters. Based on our results, we conclude that the transition from planar and ring structures to 3D cages occurs at larger cluster sizes than in the neutral system.

Since hollow cagelike geometries are frequently observed in clusters, we performed structural searches specifically aimed at low-density crystalline phases of ZnO, leading to the discovery of 57 low-density ZnO polymorphs. Many of these phases are composed of cagelike building blocks, some of which had not been considered for zeolite structures. Our topological analysis shows that many of the building blocks in these low-density phases are indeed found in small clusters $(ZnO)_n$ with sizes ranging from $n = 4$ to $n = 16$. Since these voids are large enough to accommodate guest atoms, the materials properties could be tuned by trapping different atomic species in the voids for various potential applications.

ACKNOWLEDGMENTS

M.A. acknowledges support from the Novartis Universität Basel Excellence Scholarship for Life Sciences and the Swiss National Science Foundation (Projects No. P300P2-158407 and No. P300P2-174475). Computing resources from the following centers are gratefully acknowledged: the Swiss

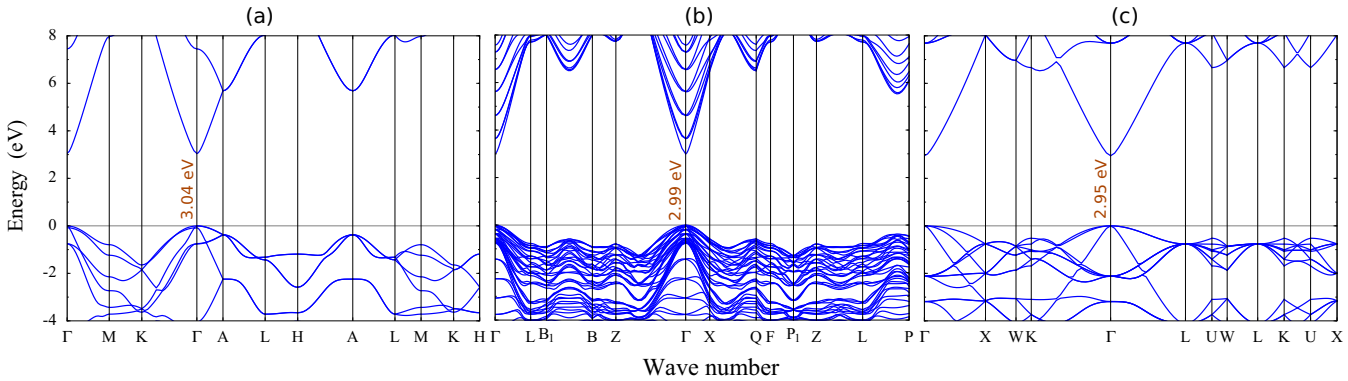

FIG. 11. The shifted PBE electronic band structures for (a) WZ, (b) C01, and (c) ZB together with the values of the band gaps. The Fermi level is denoted by the horizontal line.

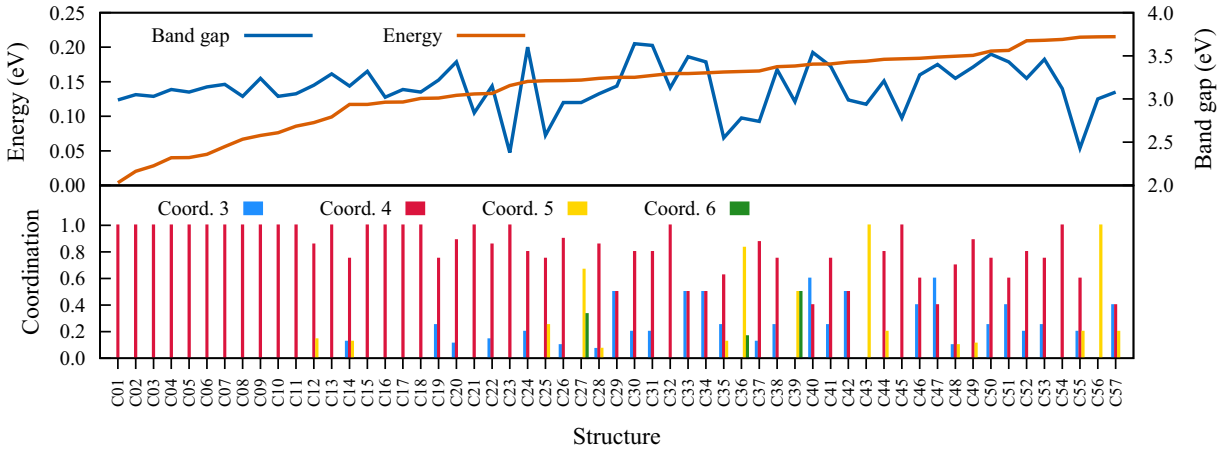

FIG. 12. The top panel shows the band gaps and energies with respect to the ground-state structure for all new polymorphs of ZnO. The bottom panel shows a histogram of the normalized fraction of Zn atoms coordinated with three, four, five, and six O atoms for every polymorph.

National Supercomputing Center in Lugano (Project s700), the Extreme Science and Engineering Discovery Environment (XSEDE) (which is supported by the National Science Foundation through Grant No. OCI-1053575), the Bridges system at the Pittsburgh Supercomputing Center (PSC) (which is supported by NSF Award No. ACI-1445606), the Quest high performance computing facility at Northwestern University, and the National Energy Research Scientific Computing Center (U.S. Department of Energy under Contract No. DE-AC02-05CH11231).

[1] A. Moezzi, A. M. McDonagh, and M. B. Cortie, Chem. Eng. J. **185**, 1 (2012).
[2] N. Padmavathy and R. Vijayaraghavan, Sci. Technol. Adv. Mater. **9**, 035004 (2008).
[3] A. H. Battez, R. González, J. Viesca, J. Fernández, J. D. Fernández, A. Machado, R. Chou, and J. Riba, Wear **265**, 422 (2008).
[4] R. A. Powell, W. E. Spicer, and J. C. McMenamin, Phys. Rev. Lett. **27**, 97 (1971).
[5] R. A. Powell, W. E. Spicer, and J. C. McMenamin, Phys. Rev. B **6**, 3056 (1972).
[6] V. Srikant and D. R. Clarke, J. Appl. Phys. **83**, 5447 (1998).
[7] Ü. Özgür, Y. I. Alivov, C. Liu, A. Teke, M. A. Reshchikov, S. Doğan, V. Avrutin, S.-J. Cho, and H. Morkoç, J. Appl. Phys. **98**, 041301 (2005).
[8] B.-Y. Oh, M.-C. Jeong, T.-H. Moon, W. Lee, J.-M. Myoung, J.-Y. Hwang, and D.-S. Seo, J. Appl. Phys. **99**, 124505 (2006).
[9] F. Ruske, C. Jacobs, V. Sittinger, B. Szyszka, and W. Werner, Thin Solid Films **515**, 8695 (2007).
[10] Q. Zhang, K. Park, and G. Cao, Mater. Matters **5**, 32 (2010).
[11] Q. Zhang, T. Chou, B. Russo, S. Jenekhe, and G. Cao, Angew. Chem., Int. Ed. **47**, 2402 (2008).
[12] G. Malloci, L. Chiodo, A. Rubio, and A. Mattoni, J. Phys. Chem. C **116**, 8741 (2012).
[13] J. J. Cavaleri, D. E. Skinner, D. P. Colombo, and R. M. Bowman, J. Chem. Phys. **103**, 5378 (1995).
[14] E. A. Meulenkamp, J. Phys. Chem. B **102**, 7764 (1998).
[15] D. Tainoff, B. Masenelli, O. Boisron, G. Guiraud, and P. Mélinon, J. Phys. Chem. C **112**, 12623 (2008).
[16] H. Liu, Y. Ding, M. Somayazulu, J. Qian, J. Shu, D. Häusermann, and H.-k. Mao, Phys. Rev. B **71**, 212103 (2005).
[17] P. S. Sokolov, A. N. Baranov, Z. V. Dobrokhotov, and V. L. Solozhenko, Russian Chemical Bulletin **59**, 325 (2010).
[18] M. Hellström, K. Jorner, M. Bryngelsson, S. E. Huber, J. Kullgren, T. Frauenheim, and P. Broqvist, J. Phys. Chem. C **117**, 17004 (2013).
[19] A. Alvarado, J. Attapattu, Y. Zhang, and C. Chen, J. Appl. Phys. **118**, 165101 (2015).
[20] S.-K. Kim, S.-Y. Jeong, and C.-R. Cho, Appl. Phys. Lett. **82**, 562 (2003).
[21] A. B. M. A. Ashrafi, A. Ueta, A. Avramescu, H. Kumano, I. Suemune, Y.-W. Ok, and T.-Y. Seong, Appl. Phys. Lett. **76**, 550 (2000).
[22] Y. Mori, N. Niiya, K. Ukegawa, T. Mizuno, K. Takarabe, and A. L. Ruoff, Phys. Status Solidi B **241**, 3198 (2004).
[23] A. Matei, I. Cernica, O. Cadar, C. Roman, and V. Schiopu, Int. J. Material Forming **1**, 767 (2008).
[24] D. Vaishnav and R. K. Goyal, IOP Conf. Ser.: Mater. Sci. Eng. **64**, 012016 (2014).
[25] E. C. Behrman, R. K. Foehrweiser, J. R. Myers, B. R. French, and M. E. Zandler, Phys. Rev. A **49**, R1543 (1994).
[26] M. Zandler, E. Behrman, M. Arrasmith, J. Myers, and T. Smith, J. Mol. Struct. (THEOCHEM) **362**, 215 (1996).
[27] J. M. Matxain, J. E. Fowler, and J. M. Ugalde, Phys. Rev. A **62**, 053201 (2000).
[28] J. M. Matxain, J. M. Mercero, J. E. Fowler, and J. M. Ugalde, J. Am. Chem. Soc. **125**, 9494 (2003).
[29] B. Wang, S. Nagase, J. Zhao, and G. Wang, J. Phys. Chem. C **111**, 4956 (2007).
[30] I. A. Sarsari, S. J. Hashemifar, and H. Salamati, J. Phys.: Condens. Matter **24**, 505502 (2012).
[31] B. Wang, X. Wang, G. Chen, S. Nagase, and J. Zhao, J. Chem. Phys. **128**, 144710 (2008).

[32] Z. Zhu, A. Chutia, R. Sahnoun, M. Koyama, H. Tsuboi, N. Hatakeyama, A. Endou, H. Takaba, M. Kubo, C. A. D. Carpio, and A. Miyamoto, Jpn. J. Appl. Phys. **47**, 2999 (2008).

[33] J.-O. Joswig, S. Roy, P. Sarkar, and M. Springborg, Chem. Phys. Lett. **365**, 75 (2002).

[34] M. Chen, T. P. Straatsma, Z. Fang, and D. A. Dixon, J. Phys. Chem. C **120**, 20400 (2016).

[35] J. Wang, A. J. Kulkarni, K. Sarasamak, S. Limpijumnong, F. J. Ke, and M. Zhou, Phys. Rev. B **76**, 172103 (2007).

[36] J. Carrasco, F. Illas, and S. T. Bromley, Phys. Rev. Lett. **99**, 235502 (2007).

[37] M. A. Zwijnenburg, F. Illas, and S. T. Bromley, Phys. Rev. Lett. **104**, 175503 (2010).

[38] D. Zagorac, J. C. Schön, J. Zagorac, and M. Jansen, Phys. Rev. B **89**, 075201 (2014).

[39] P. Guo, J. Shin, A. G. Greenaway, J. G. Min, J. Su, H. J. Choi, L. Liu, P. A. Cox, S. B. Hong, P. A. Wright, and X. Zou, Nature (London) **524**, 74 (2015).

[40] I. Demiroglu, S. Tosoni, F. Illas, and S. T. Bromley, Nanoscale **6**, 1181 (2014).

[41] A. A. Al-Sunaidi, A. A. Sokol, C. R. A. Catlow, and S. M. Woodley, J. Phys. Chem. C **112**, 18860 (2008).

[42] S. A. Ghasemi, A. Hofstetter, S. Saha, and S. Goedecker, Phys. Rev. B **92**, 045131 (2015).

[43] S. Faraji, S. A. Ghasemi, S. Rostami, R. Rasoulkhani, B. Schaefer, S. Goedecker, and M. Amsler, Phys. Rev. B **95**, 104105 (2017).

[44] K. Koyasu, K. Komatsu, and F. Misaizu, J. Chem. Phys. **139**, 164308 (2013).

[45] A. V. Bulgakov, A. B. Evtushenko, Y. G. Shukhov, I. Ozerov, and W. Marine, Appl. Phys. A: Mater. Sci. Process. **101**, 585 (2010).

[46] S. Goedecker, J. Chem. Phys. **120**, 9911 (2004).

[47] S. Roy, S. Goedecker, and V. Hellmann, Phys. Rev. E **77**, 056707 (2008).

[48] S. E. Schönborn, S. Goedecker, S. Roy, and A. R. Oganov, J. Chem. Phys. **130**, 144108 (2009).

[49] M. Amsler and S. Goedecker, J. Chem. Phys. **133**, 224104 (2010).

[50] B. Schaefer, S. A. Ghasemi, S. Roy, and S. Goedecker, J. Chem. Phys. **142**, 034112 (2015).

[51] E. Bitzek, P. Koskinen, F. Gähler, M. Moseler, and P. Gumbsch, Phys. Rev. Lett. **97**, 170201 (2006).

[52] C. G. Broyden, IMA J. Appl. Math. **6**, 76 (1970).

[53] R. Fletcher, Comput. J. **13**, 317 (1970).

[54] M. Sicher, S. Mohr, and S. Goedecker, J. Chem. Phys. **134**, 044106 (2011).

[55] S. Roy, S. Goedecker, M. J. Field, and E. Penev, J. Phys. Chem. B **113**, 7315 (2009).

[56] F. Jensen, *Introduction to Computational Chemistry*, 2nd ed. (John Wiley, New York, 2011).

[57] A. Willand, M. Gramzow, S. A. Ghasemi, L. Genovese, T. Deutsch, K. Reuter, and S. Goedecker, Phys. Rev. B **81**, 201405(R) (2010).

[58] M. Amsler, J. A. Flores-Livas, L. Lehtovaara, F. Balima, S. A. Ghasemi, D. Machon, S. Pailhès, A. Willand, D. Caliste, S. Botti, A. San Miguel, S. Goedecker, and M. A. L. Marques, Phys. Rev. Lett. **108**, 065501 (2012).

[59] T. D. Huan, M. Amsler, V. N. Tuoc, A. Willand, and S. Goedecker, Phys. Rev. B **86**, 224110 (2012).

[60] S. Botti, M. Amsler, J. A. Flores-Livas, P. Ceria, S. Goedecker, and M. A. L. Marques, Phys. Rev. B **88**, 014102 (2013).

[61] T. D. Huan, M. Amsler, R. Sabatini, V. N. Tuoc, N. B. Le, L. M. Woods, N. Marzari, and S. Goedecker, Phys. Rev. B **88**, 024108 (2013).

[62] M. Amsler, S. S. Naghavi, and C. Wolverton, Chem. Sci. **8**, 2226 (2017).

[63] S. M. Clarke, M. Amsler, J. P. S. Walsh, T. Yu, Y. Wang, Y. Meng, S. D. Jacobsen, C. Wolverton, and D. E. Freedman, Chem. Mater. **29**, 5276 (2017).

[64] M. Amsler, S. Botti, M. A. L. Marques, T. J. Lenosky, and S. Goedecker, Phys. Rev. B **92**, 014101 (2015).

[65] B. Aradi, B. Hourahine, and T. Frauenheim, J. Phys. Chem. A **111**, 5678 (2007).

[66] N. H. Moreira, G. Dolgonos, B. Aradi, A. L. da Rosa, and T. Frauenheim, J. Chem. Theory Comput. **5**, 605 (2009).

[67] J. Behler, J. Chem. Phys. **134**, 074106 (2011).

[68] V. Blum, R. Gehrke, F. Hanke, P. Havu, V. Havu, X. Ren, K. Reuter, and M. Scheffler, Comput. Phys. Commun. **180**, 2175 (2009).

[69] J. P. Perdew, K. Burke, and M. Ernzerhof, Phys. Rev. Lett. **77**, 3865 (1996).

[70] L. Genovese, A. Neelov, S. Goedecker, T. Deutsch, S. A. Ghasemi, A. Willand, D. Caliste, O. Zilberberg, M. Rayson, A. Bergman, and R. Schneider, J. Chem. Phys. **129**, 014109 (2008).

[71] L. Genovese, T. Deutsch, A. Neelov, S. Goedecker, and G. Beylkin, J. Chem. Phys. **125**, 074105 (2006).

[72] S. Goedecker, M. Teter, and J. Hutter, Phys. Rev. B **54**, 1703 (1996).

[73] C. Hartwigsen, S. Goedecker, and J. Hutter, Phys. Rev. B **58**, 3641 (1998).

[74] J. P. Perdew, M. Ernzerhof, and K. Burke, J. Chem. Phys. **105**, 9982 (1996).

[75] C. Adamo and V. Barone, J. Chem. Phys. **110**, 6158 (1999).

[76] A. D. Becke, J. Chem. Phys. **98**, 5648 (1993).

[77] A. Togo and I. Tanaka, Scr. Mater. **108**, 1 (2015).

[78] Y. Yong, B. Song, and P. He, J. Phys. Chem. C **115**, 6455 (2011).

[79] S. M. Woodley, M. B. Watkins, A. A. Sokol, S. A. Shevlin, and C. R. A. Catlow, Phys. Chem. Chem. Phys. **11**, 3176 (2009).

[80] A. Dmytruk, I. Dmitruk, I. Blonskyy, R. Belosludov, Y. Kawazoe, and A. Kasuya, Microelectron. J. **40**, 218 (2009).

[81] X. Wang, B. Wang, L. Tang, L. Sai, and J. Zhao, Phys. Lett. A **374**, 850 (2010).

[82] R. Xu, W. Pang, J. Yu, Q. Huo, and J. Chen, *Chemistry of Zeolites and Related Porous Materials: Synthesis and Structure* (John Wiley & Sons, New York, 2009).

[83] E. V. Trushin, I. L. Zilberberg, and A. V. Bulgakov, Phys. Solid State **54**, 859 (2012).

[84] O. O. Kurakevych, T. A. Strobel, D. Y. Kim, T. Muramatsu, and V. V. Struzhkin, Cryst. Growth Des. **13**, 303 (2013).

[85] D. Y. Kim, S. Stefanoski, O. O. Kurakevych, and T. A. Strobel, Nat. Mater. **14**, 169 (2015).

[86] L. Sponza, J. Goniakowski, and C. Noguera, Phys. Rev. B **91**, 075126 (2015).

[87] M. A. Zwijnenburg and S. T. Bromley, Phys. Rev. B **83**, 024104 (2011).
[88] L. Zhu, M. Amsler, T. Fuhrer, B. Schaefer, S. Faraji, S. Rostami, S. A. Ghasemi, A. Sadeghi, M. Grauzinyte, C. Wolverton, and S. Goedecker, J. Chem. Phys. **144**, 034203 (2016).
[89] G. S. Oleinik and N. V. Danilenko, Russ. Chem. Rev. **66**, 553 (1997).
[90] U. Muller, *Inorganic Structural Chemistry* (Wiley, Hoboken, NJ, 2007).
[91] W. Sangthong, J. Limtrakul, F. Illas, and S. T. Bromley, Phys. Chem. Chem. Phys. **12**, 8513 (2010).
[92] J. E. Jaffe, J. A. Snyder, Z. Lin, and A. C. Hess, Phys. Rev. B **62**, 1660 (2000).
[93] L. M. Ch. Baerlocher, "Database of Zeolite Structures", http://www.iza-structure.org/databases/.
[94] Z. Liu, X. Wang, J. Cai, G. Liu, P. Zhou, K. Wang, and H. Zhu, J. Phys. Chem. C **117**, 17633 (2013).
[95] V. N. Tuoc, T. D. Huan, N. V. Minh, and N. T. Thao, J. Phys.: Conf. Ser. **726**, 012022 (2016).
[96] See Supplemental Material at http://link.aps.org/supplemental/10.1103/PhysRevB.96.064108 for structural data, phonon dispersion, and electronic band structures of all clusters and crystalline polymorphs discussed here.
[97] H. D. Tran, M. Amsler, S. Botti, M. A. L. Marques, and S. Goedecker, J. Chem. Phys. **140**, 124708 (2014).
[98] C. L. Freeman, F. Claeyssens, N. L. Allan, and J. H. Harding, Phys. Rev. Lett. **96**, 066102 (2006).
[99] D. Zagorac, J. C. Schön, and M. Jansen, J. Phys. Chem. C **116**, 16726 (2012).
[100] C. Tusche, H. L. Meyerheim, and J. Kirschner, Phys. Rev. Lett. **99**, 026102 (2007).
[101] W. Y. Liang and A. D. Yoffe, Phys. Rev. Lett. **20**, 59 (1968).
[102] H. Kumano, A. Ashrafi, A. Ueta, A. Avramescu, and I. Suemune, J. Cryst. Growth **214**, 280 (2000).